Electronic Supplementary Information (ESI)

Solvophobic-controlled synthesis of smart magneto-fluorescent superstructures for real-time inspection of metallic fractures

Fernando Menegatti de Melo [a,b]*, João V. Mattioni[a], Fernando Dias[b], Ying Fu[c], Henrique E. Toma[a]

[a.]*Supramolecular Nanotech Laboratory, Institute of Chemistry, University of São Paulo, Avenida Professor Lineu Prestes, 748, 05508000, São Paulo, Brazil.*

[b.]*Metal-Chek do Brasil Indústria e Comércio, Research & Development Department, Rua das Indústrias, 135, 12926674, Bragança Paulista, Brazil.*

[c.]*School of Information Technology, Halmstad University, SE-30118 Halmstad, Sweden*

Keywords: quantum dots, magnetic nanoparticles, solvophobic-controlled synthesis, magneto-fluorescent nanoparticles, real-time inspection, non-destructive testing

***Corresponding Author:** fernando.menegatti.melo@usp.br

Abstract: The production of materials that contain more than one functional constituent, the so-called multifunctional materials, are quite relevant in advanced technology. By acting as building blocks, nanoparticles, resembling artificial atoms, can be suitable explored for generating higher-order multifunctional structures. In this regard, herein, a special clustered magneto-fluorescent superstructure has been developed for a non-destructive detection of flaws and shallow subsurface discontinuities in industrial ferromagnetic materials. The strategy consists in the solvophobic-controlled assembly of organic-based maghemite cores and water-based II-VI quantum dots, in the presence of hexadecyltrimethyl-ammonium bromide as a compatibilizer agent. This composite exhibited high magnetic response (s_{max} = 66 emu.g^{-1}), uniform sizes and long-term colloidal stability, in addition to tunable optical properties (QY = 78%). The strategy of utilizing nanoparticles as magneto-fluorescent nanoprobes to identify tiny slits represents a great advance, for improving the capability of precisely revealing the fracture boundary locations by visual real-time inspection. The nanoscale probes exhibit a low signal-to-noise ratio and a higher competitive performance in relation to the existing micrometric detection systems.

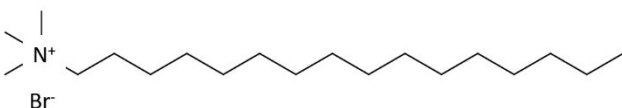# Summary of chemical and molecular formula of the main chemical reactants used in this manuscript

Magnetite (MgNP): Fe_3O_4
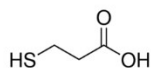
Maghemite (MghNP): $\gamma\text{-}Fe_2O_3$

Stearate (St): $(C_{17}H_{35}COO^-)$
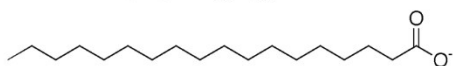
Hexadecyltrimethyl-ammonium bromide (CTAB): $C_{19}H_{42}BrN$

3-mercaptopropionate: $(C_3H_5O_2S^-)$

Iron(III) Stearate (FeSt$_3$): $(C_{54}H_{105}FeO_6)$
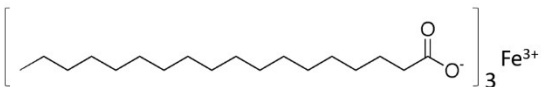
Iron(II) Stearate (FeSt$_2$): $(C_{36}H_{72}FeO_4)$
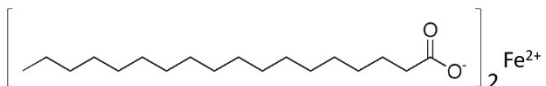
Sodium oleate (NaOl): $C_{18}H_{33}NaO_2$
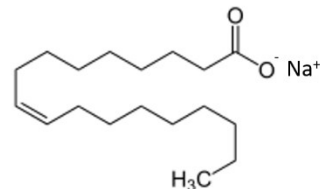
Oleic acid (HOl): $C_{18}H_{33}NaO_2$
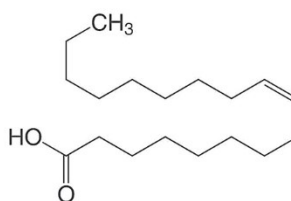
Sodium stearate (NaSt): $C_{18}H_{35}NaO_2$
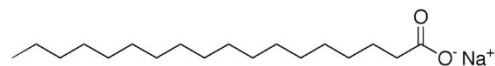
Stearic acid (HSt): $C_{18}H_{36}O_2$

HRTEM micrographs of thermal decomposition study

FeSt₂ hydrated
NaSt 100/0 HSt

FeSt₂ hydrated
NaSt 0/100 HSt

FeSt₂ dehydrated
NaSt 100/0 HSt

FeSt₂ dehydrated
NaSt 0/100 HSt
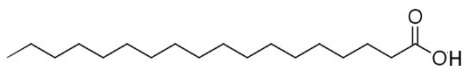
Figure S1. Influence of the ratio NaSt/HSt (100/0; 0/100) on the shape of the nanoparticles for *in house* hydrated iron(II) stearate and dehydrated iron(II) stearate. Prevalence of plate nanoparticles.

HRTEM micrographs of thermal decomposition study

FeSt$_3$ hydrated
NaSt 100/0 HSt

FeSt$_3$ hydrated
NaSt 0/100 HSt

FeSt$_3$ dehydrated
NaSt 100/0 HSt

FeSt$_3$ dehydrated
NaSt 0/100 HSt

Figure S2. Influence of the ratio NaSt/HSt (100/0; 0/100) on the shape of the nanoparticles for *in house* hydrated iron(III) stearate and dehydrated iron(III) stearate. Prevalence of rods, sphere-like and plate nanoparticles.

HRTEM micrographs of thermal decomposition study

FeSt$_2$ hydrated
NaOl 100/0 HOl

FeSt$_2$ hydrated
NaOl 0/100 HOl

FeSt$_2$ dehydrated
NaOl 100/0 HOl
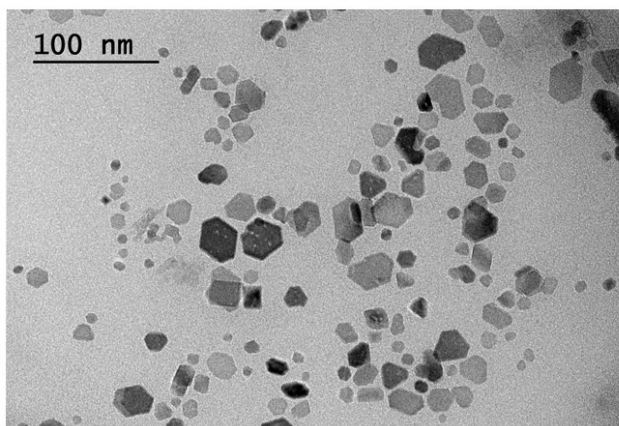
FeSt$_2$ dehydrated
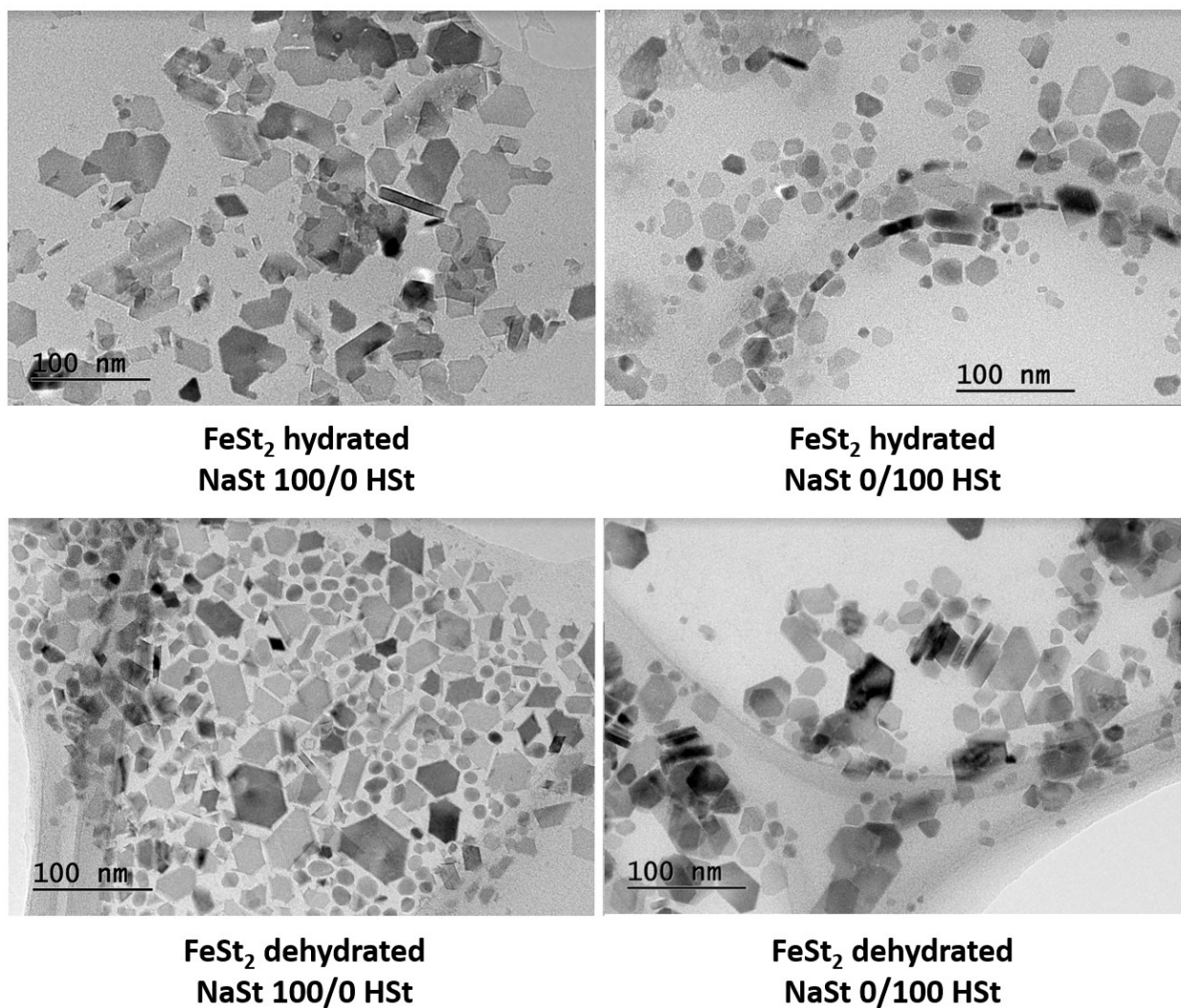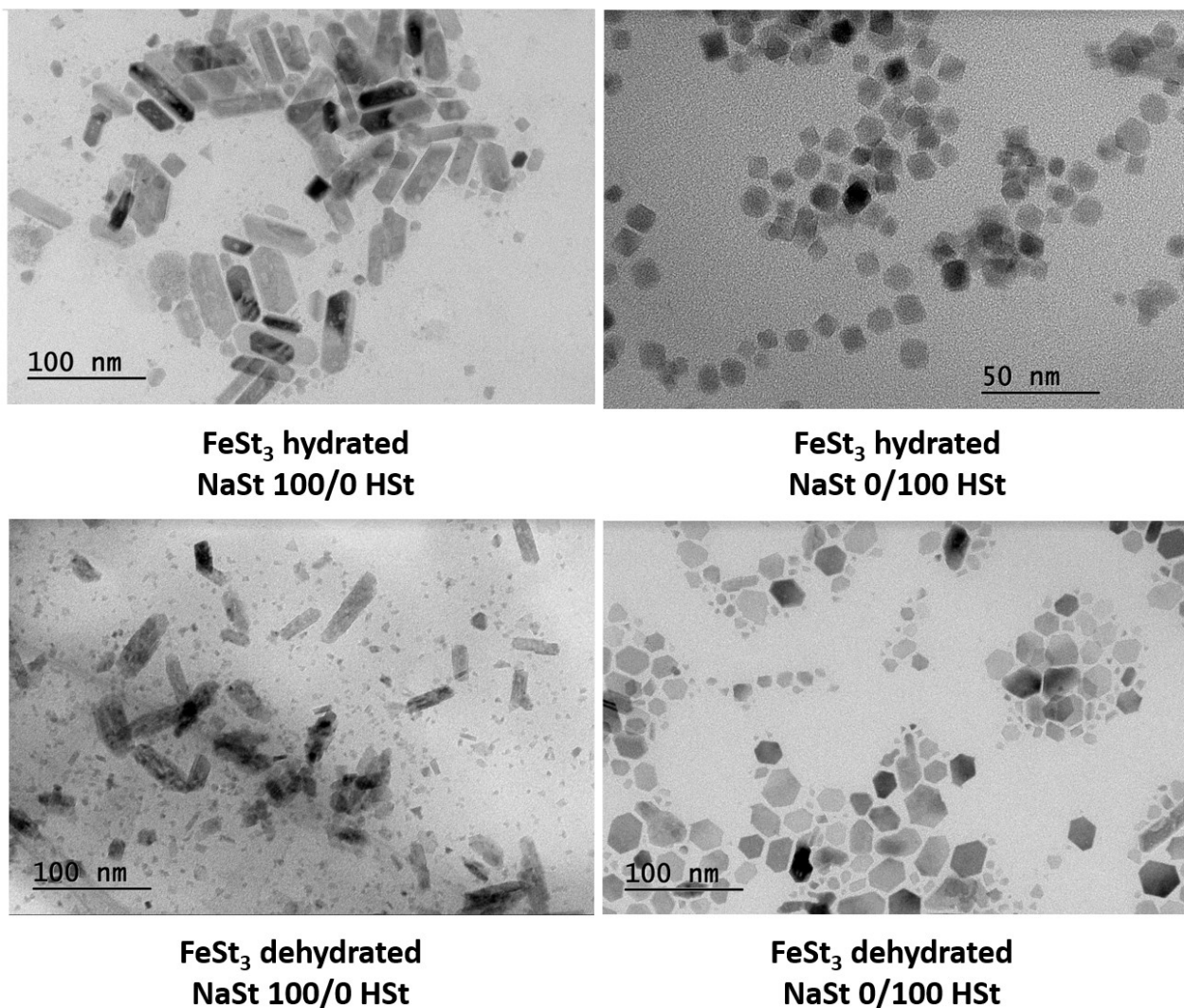**NaOl 0/100 HOl**

Figure S3. Influence of the ratio NaOl/HOl (100/0; 0/100) on the shape of the nanoparticles for *in house* hydrated iron(II) stearate and dehydrated iron(II) stearate. Prevalence sphere-like and plate nanoparticles.

HRTEM micrographs of thermal decomposition study

FeSt$_3$ hydrated
NaOl 100/0 HOl

FeSt$_3$ hydrated
NaOl 0/100 HOl

FeSt$_3$ dehydrated
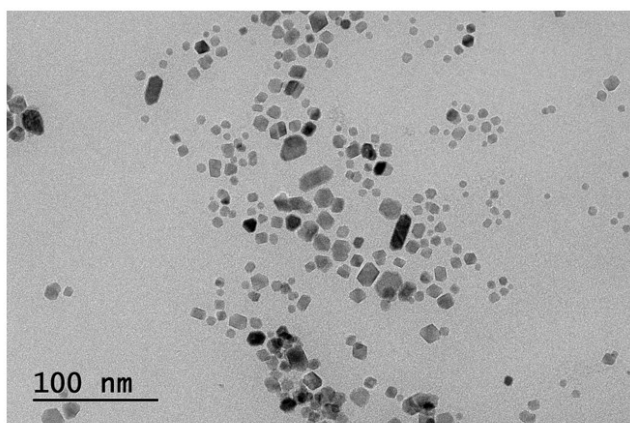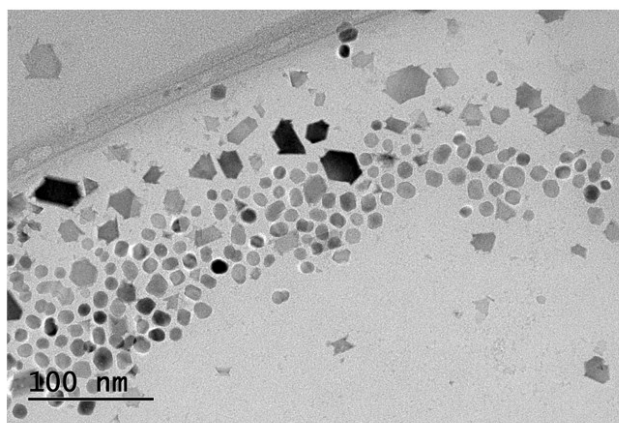NaOl 100/0 HOl

FeSt$_3$ dehydrated
NaOl 0/100 HOl

Figure S4. Influence of the ratio NaOl/HOl (100/0; 0/100) on the shape of the nanoparticles for *in house* hydrated iron(III) stearate and dehydrated iron(III) stearate. Prevalence sphere-like nanoparticles.

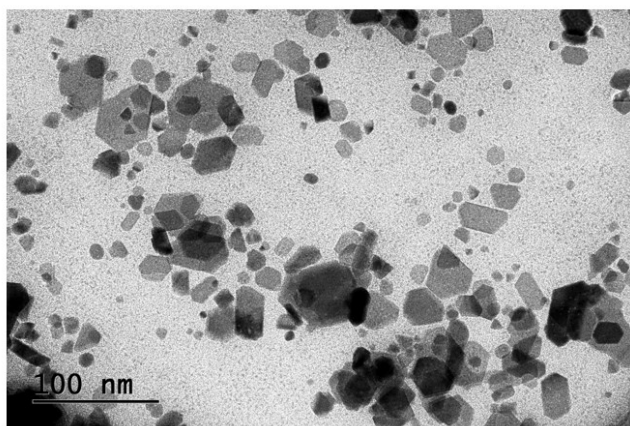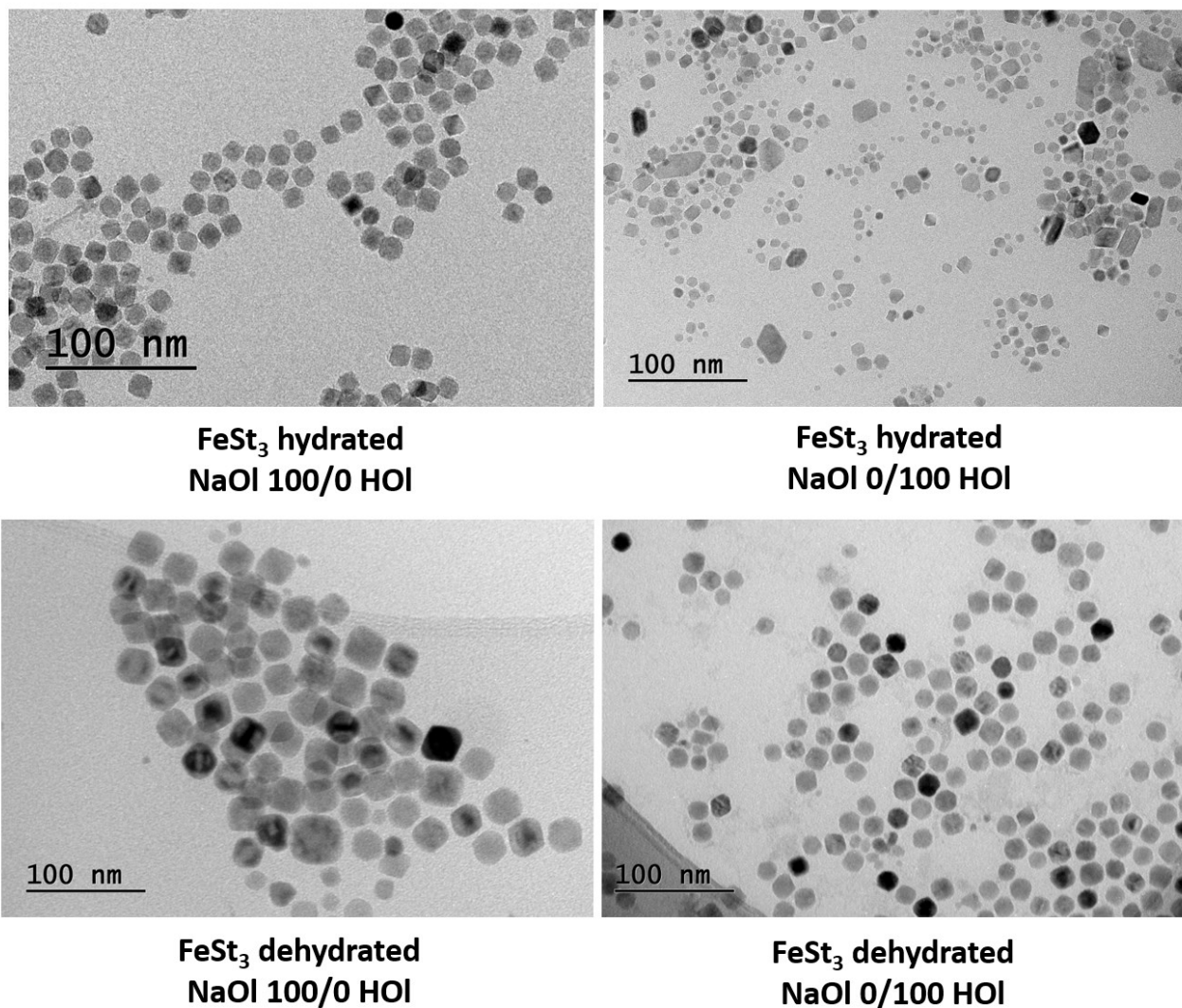# HRTEM micrographs of MgNP and MghNP
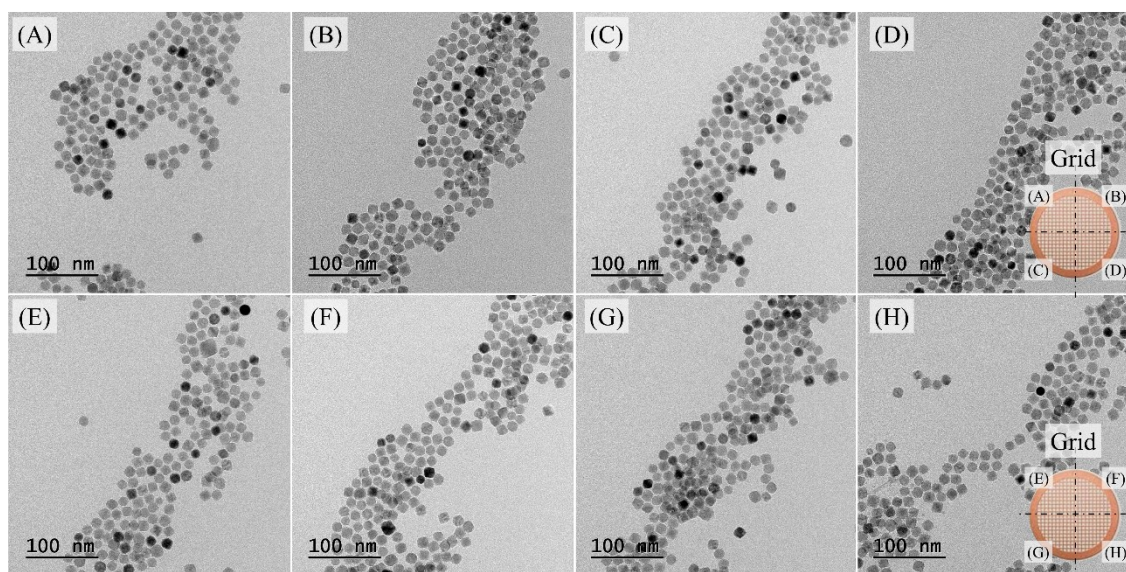
Figure S5. (A-D) TEM micrography of the quasi-spherical magnetite nanoparticles, MgNP, used to make its statistical average diameter. It was highlighted the region of the TEM grid where the micrographies were taken. (E-F) TEM micrography of the quasi-spherical maghemite nanoparticles, MghNP, used to make its statistical average diameter. It was highlighted the region of the TEM grid where the micrographies were taken.

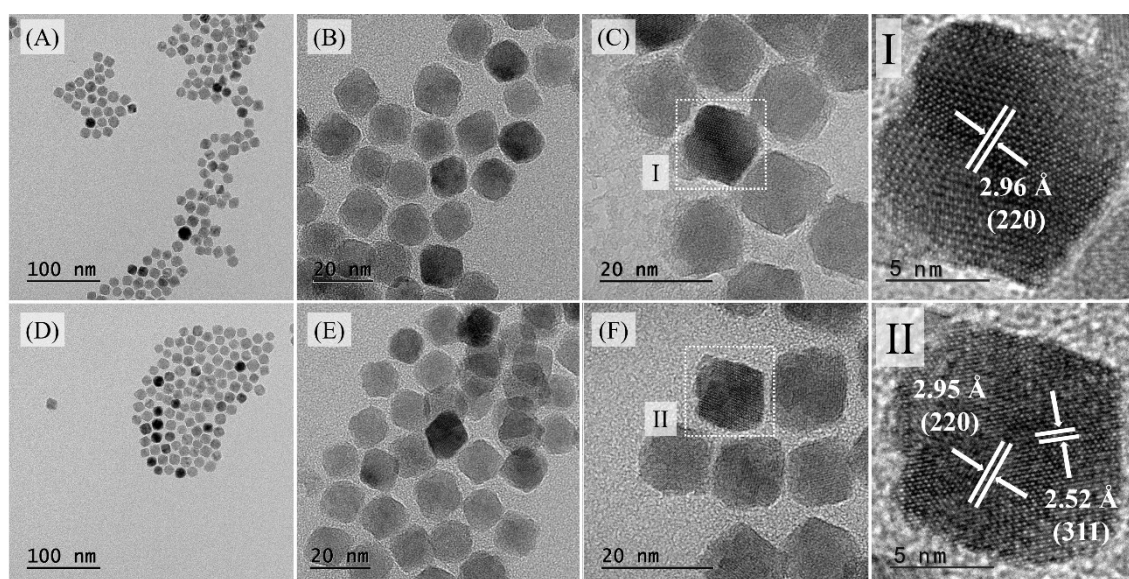**Figure S6.** (A-C) HRTEM micrography of the quasi-spherical magnetite nanoparticles, MgNP, highlighting the interplanar distance of (220) according to JCPDS 16-0629 (I). (D-F) HRTEM micrography of the quasi-spherical maghemite nanoparticles, MghNP, highlighting the interplanar distance of (220) and (311) accroding to JCPD 39-1364 (II).
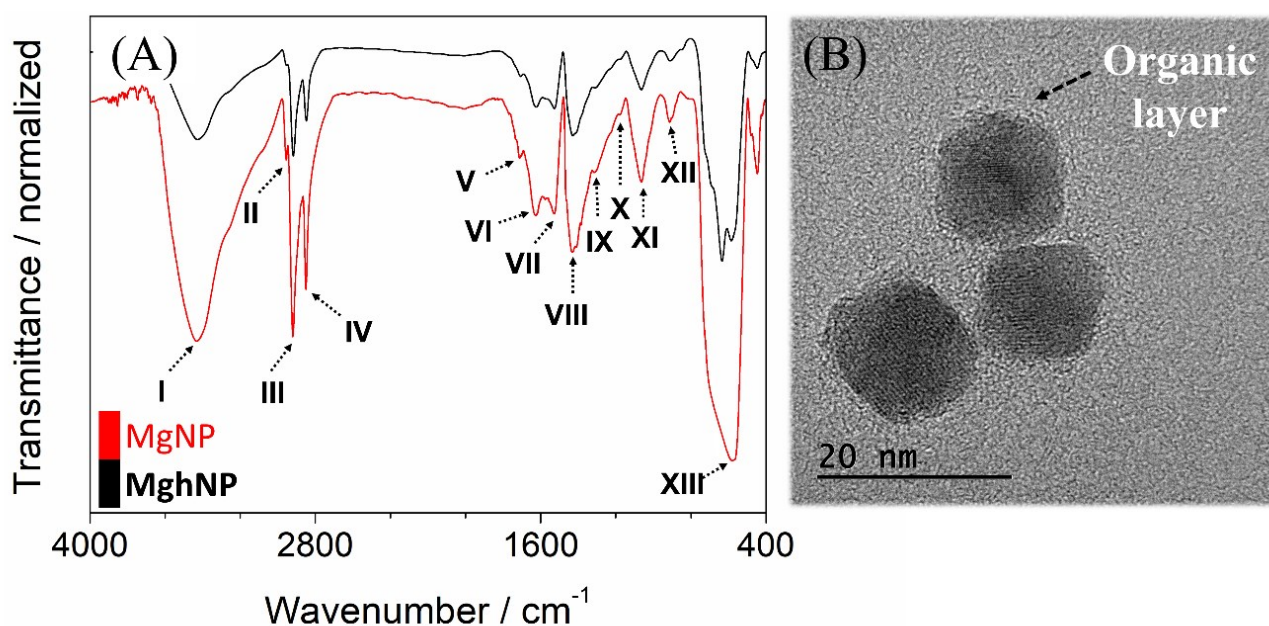
FTIR spectra of MgNP and MghNP

Figure S7. (A) FTIR spectra of MgNP and MghNP assigning the main peaks. (B) Overfocused HRTEM micrography showing the organic layer around the MghNP nanoparticles.

The intense and broad band around 3428 cm^{-1} (I) can be ascribed to O-H stretching (-COOH). This band can be observed before and after the oxidation process. The peaks at 2954 cm^{-1}(II), 2918 cm^{-1} (III) and 2849 cm^{-1} (IV), are characteristic of C-H asymmetrical and symmetrical stretching vibrations (-CH$_2$ and -CH$_3$) known as Fermi doublet. The weak peak in 1712 cm^{-1} (V) can be indicating the presence of small excess of the stearate in the nanoparticles' surface. Now, the medium peaks at 1624 cm^{-1} (VI) and 1527 cm^{-1} (VII), correspond to the asymmetrical and symmetrical vibrations of the carbonyl group (-COO$^-$). The stearate layer at the nanoparticles surfaces is a key point to the hybrid material formation, since it provides a non-polar recovering onto iron oxide nanoparticles that will interact with the CTAB non-polar chain, as discussed in the manuscript. The peaks at 1429 cm^{-1} (VIII) and 1250 cm^{-1} (IX) are characteristic of metil rocking (-CH$_3$) and carbonyl scissoring (-COO$^-$). The last four peaks 1116 cm^{-1}, 1066 cm^{-1}, 913 cm^{-1} and 583 cm^{-1}, are characteristics to C-O stretching (-COOH), C-H wagging (-CH$_2$), carbonyl bending (-COO$^-$) and Fe-O stretching (Fe$_x$O$_y$).

XRD – Rietveld Refinement of MgNP and MghNP
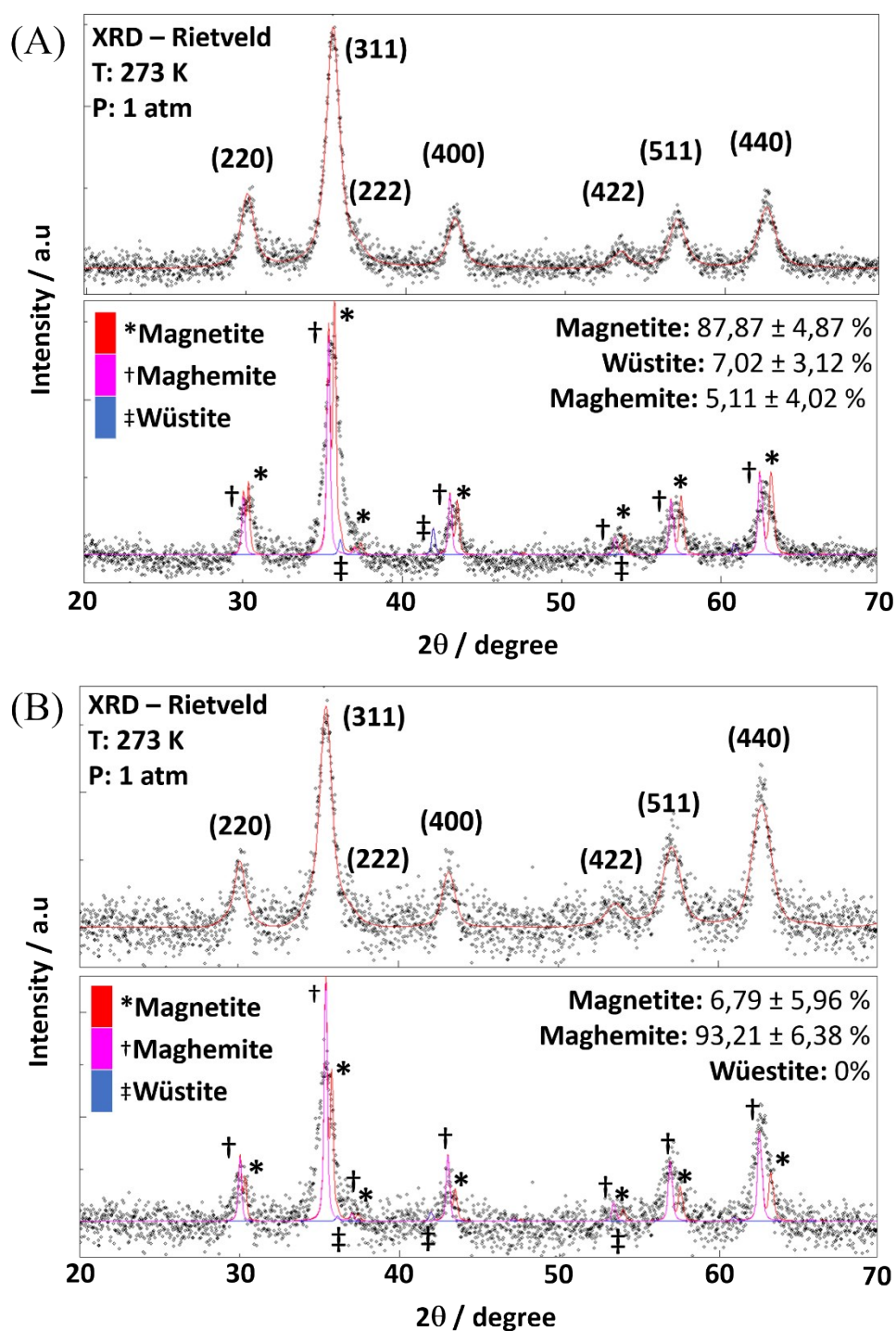
Figure S8. (A) XRD Rietveld refinement of MgNP indicating the majority amount of magnetite before the assisted oxidation. (B) XRD Rietveld refinement of MghNP indicating the majority amount of maghemite after the assisted oxidation. (Maud software 2.91 version and VESTA software 3.4.7 version were used to make the refinement and show the CIFs information respectively; sig 1.005 and Rwp 4.093)

RGB analysis of QD

(A)

(B)
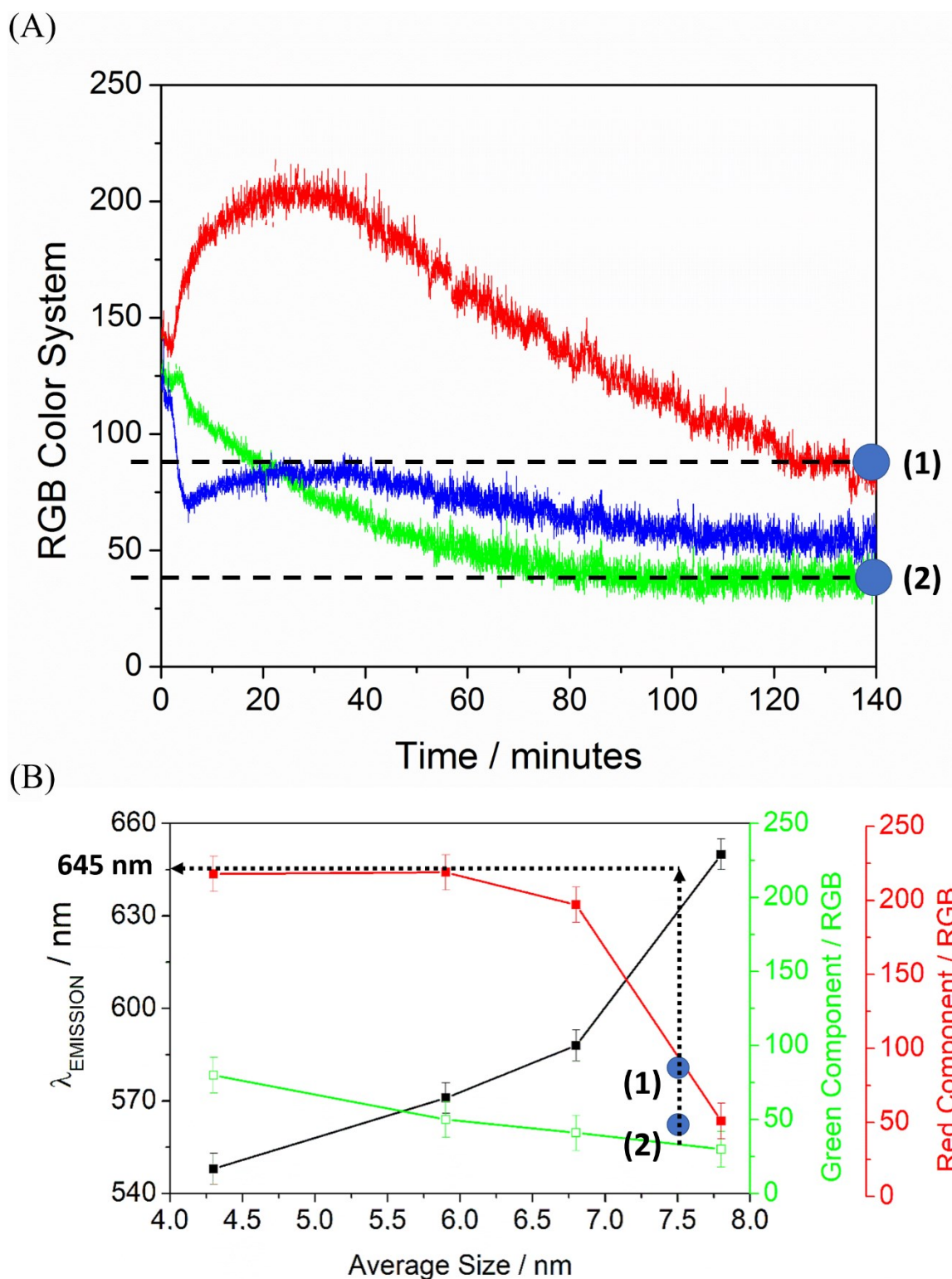
Figure S9. (A) Representative RGB spectrum in which the red, green and blue components are monitored as a function of the reaction time for our synthetic parameters. It was highlighted the final red component value (1), 79, and the final green component value, (2), 30. (B) Correlation between the variation of the red component the QD mean size and their luminescence properties. As we can see, the values (1) and (2) corroborates to 645 nm emission (very close to the experimental value, 649 nm) – this correlation plot was determined in a previous paper[1]

FTIR spectra of QD

Figure S10. (A) FTIR spectra of QD assigning the main peaks. (B) Overfocused HRTEM micrography showing the organic layer around the QD nanoparticles.

In the IR spectra the intense and broad band around 3425 cm^{-1}, peak I, can be ascribed to O-H stretching (-COOH). The weak peaks at 2964 cm^{-1} and 2933 cm^{-1}, peaks II and III respectively, are characteristic of C-H asymmetrical and symmetrical stretching vibrations (-CH$_2$). The absence o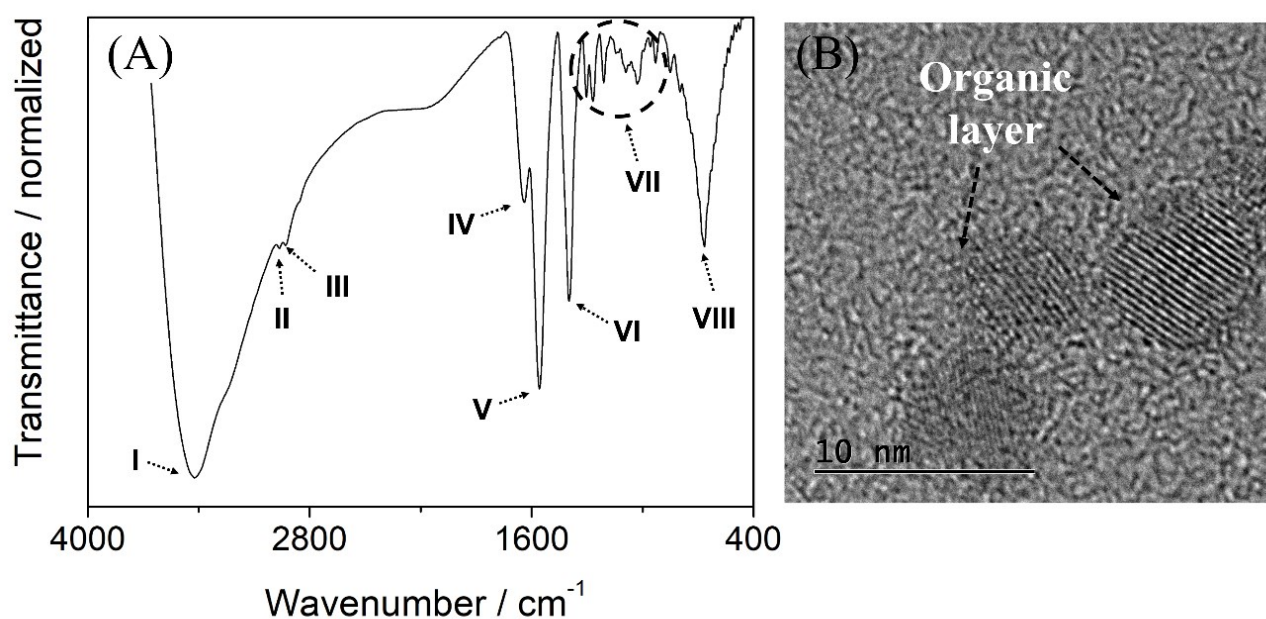f metil group decrease the peaks intensity as expected. The peak in 1638 cm^{-1}, peak IV, is superimposed to the deformation vibrational peaks of water, almost always observed in the water-based nanoparticles. Now, the strong peaks at 1587 and 1397 cm^{-1}, peaks V and VI, correspond to the asymmetrical and symmetrical vibrations of the carbonyl group (-COO$^-$) due to mercaptopropionate. The propionate layer on the nanoparticles surfaces is another key point to the hybrid material formation, since it provides a charged recovering onto quantum dots nanoparticles that will interact with the CTAB charged head, as discussed in the manuscript. The peaks signed as VII are related to carbonyl scissoring (-COO$^-$), to C-O stretching (-COOH), C-H wagging (-CH$_2$) and carbonyl bending (-COO$^-$). The last peak in 665 cm^{-1} is attributed to Cd-S stretching due to the covalent interaction between the ligand and inorganic core.

TEM micrographies of multi-magnetic core of MghNP
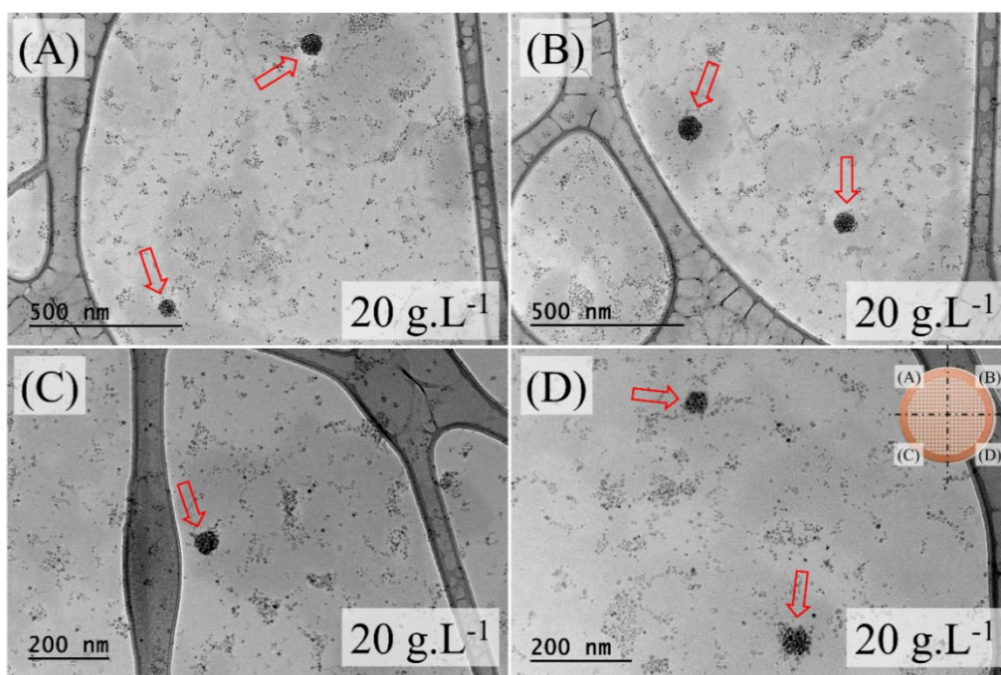
Figure S11. (A-D) TEM micrography of the quasi-spherical MghNP using 20 g.L^{-1} CTAB. It is possible to see some multi-magnetic core nanoparticles, MghNP-micele. It was highlighted the region of the TEM grid where the micrographies were taken (D, inset).
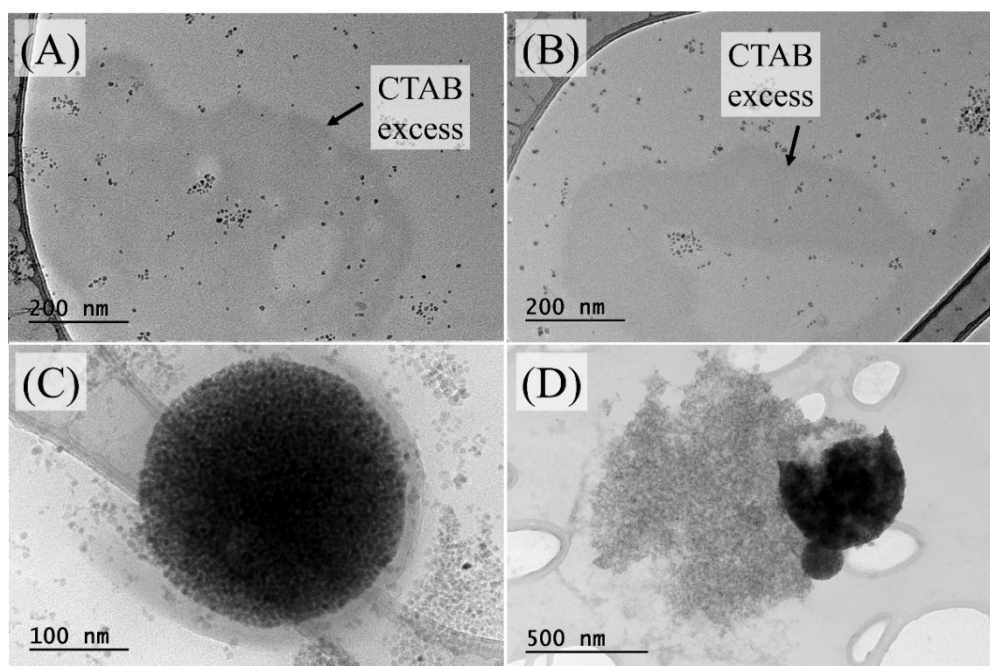
Figure S12. TEM micrography of the multi-magnetic core of MghNP in different organic-based magnetic nanoparticles:CTAB ratio. (A-B) 25 g.L^{-1} CTAB and 2.0 g.L^{-1} MghNP showing CTAB excess. (C-D) 10 g.L^{-1} CTAB and 4.5 g.L^{-1} MghNP in different regions.

Average size of magneto-fluorescent nanocomposites (MghNP@QD) in acetone

Average size = 117,0 ± 4,8 nm
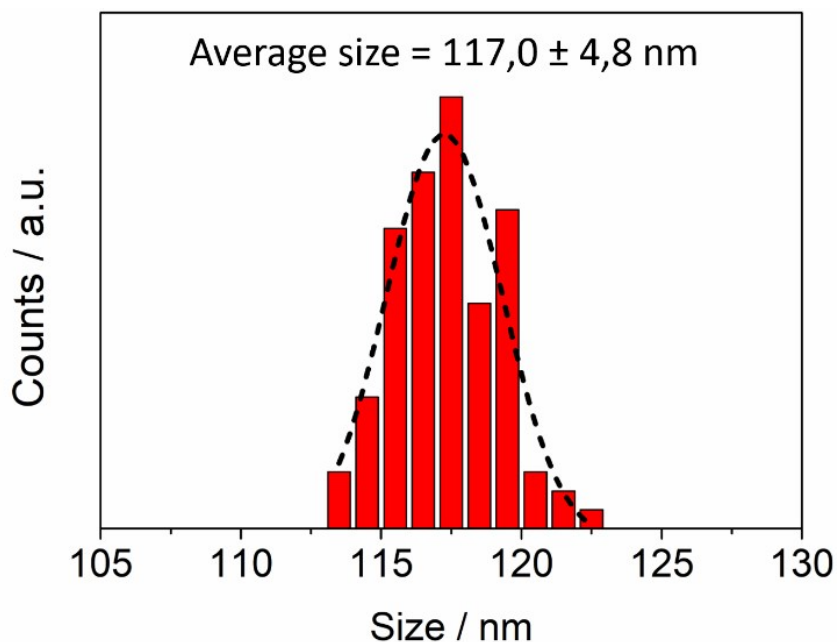
Figure S13. DLS measurement of magneto-fluorescent nanocomposites, MghNP@QD, indicating its average size.

Despite the zeta potential of this magneto-fluorescent composites is slightly negative (almost – 4,0 mV measured in water) because of the quantum dots recovering and the cancellation of the positive charge coming from the magnetic core (+ 30 mV), there is no reason to report pH since the medium where DLS was measured is acetone and not water. Moreover, because of the chemical nature of the magneto-fluorescent composite formation, the electrostatic force can be break under water washing. It is going to separate magnetic content and fluorescent one as we pointed out.

Quantum Yield of QD and MghNP@QD

The UV-vis absorbance spectrum of the solvent background (water) was recorded for the chosen sample. After that, the fluorescence spectrum of the same solution in the 10 mm fluorescence cuvette was taken too. Calculate and note down the integrated fluorescence intensity from the fully corrected fluorescence spectrum. This procedure was repeated for five solutions with increasing concentrations of the chosen sample. (There will be six solutions in all, corresponding to absorbance at the excitation wavelength of ~0/solvent blank, 0.02, 0.04, 0.06, 0.08 and 0.10.) In this way, a graph of integrated fluorescence *intensity vs absorbance* was plotted. The result should be a straight line with gradient, Coef, and intercept = 0. The quantum yield calculus is made from a known standard sample quantum yield by means of the following equation:

$$\Phi_{sample} = \Phi_{standard}\left(\frac{Coef_{sample}}{Coef_{standard}}\right)\left(\frac{\eta_{sample}^{2}}{\eta_{standard}^{2}}\right)$$

It is important to use two standard samples (Fluorescein and Rodamine 6G were used as standard samples; 0.79 and 0.95 respectively) and take one of them as a problem sample just to confirm the quantum yield value. Using both standard samples, we calculated an average quantum yield to CdTe quantum dots as 84% and to MghNP@QD as 78%. However, the stabilization of the MghNP@QD in solution is not so high. In that way, we had to optimize the integration time of the PL and Abs measurement, and the concentration, to be possible to make the calculation. It is important to say that, when we use water to redisperse this material, we are going to favor the breaking electrostatic force between QD and magnetic core. The iterative reprecipitation form again the composite. This procedure guarantees the elimination of ligands that are in the middle of the QDs and magnetic core and are not bonded. The magnetic separation is not able to do that.

Superparamagnetism *vs* Monodomain

As Mathew et al, 2007 reported, domains which are groups of spins all pointing in the same direction are separated by domain walls, which have a characteristic width and energy. They mention that the coercivity Hc increases with decreasing grain size D down to values of about 40 nm, independent of the kind of material. The increase of Hc is proportional to $1/D$. The reason for this is that in small particles the formation of a closed magnetic flux becomes energetically less favorable so that the magnetic domain size with a uniform magnetization becomes more and more identical with the grain size. This grain size is defined as the first critical size (Dc, which is characteristic of each material) where the multidomain materials change to a monodomain material. This leads to a strong increase of the coercivity because a change of magnetization in this case cannot happen only by shifting the domain walls which normally requires only a weak magnetic field. As the size of magnetic element scales below 20 nm, the transformation from ferromagnetic to superparamagnetic behavior occurs. In the superparamagnetic state of the material, the room temperature thermal energy overcomes the magnetostatic energy well of the domain or the particle, resulting in zero hysteresis. In other words, although the particle itself is a single domain ferromagnet, the ability of an individual magnetic "dot" to store magnetization orientation information is lost when its dimension is below a threshold. Consequently, the magnetic moments within a particle rotate rapidly in unison, exhibiting the superparamagnetic relation phenomenon.[2] Therefore, monodomain particles not necessarily show superparamagnetic behavior. That was the reason why we decided to use small nanoparticles and promote their agglomeration instead of using monodomain nanoparticles only.
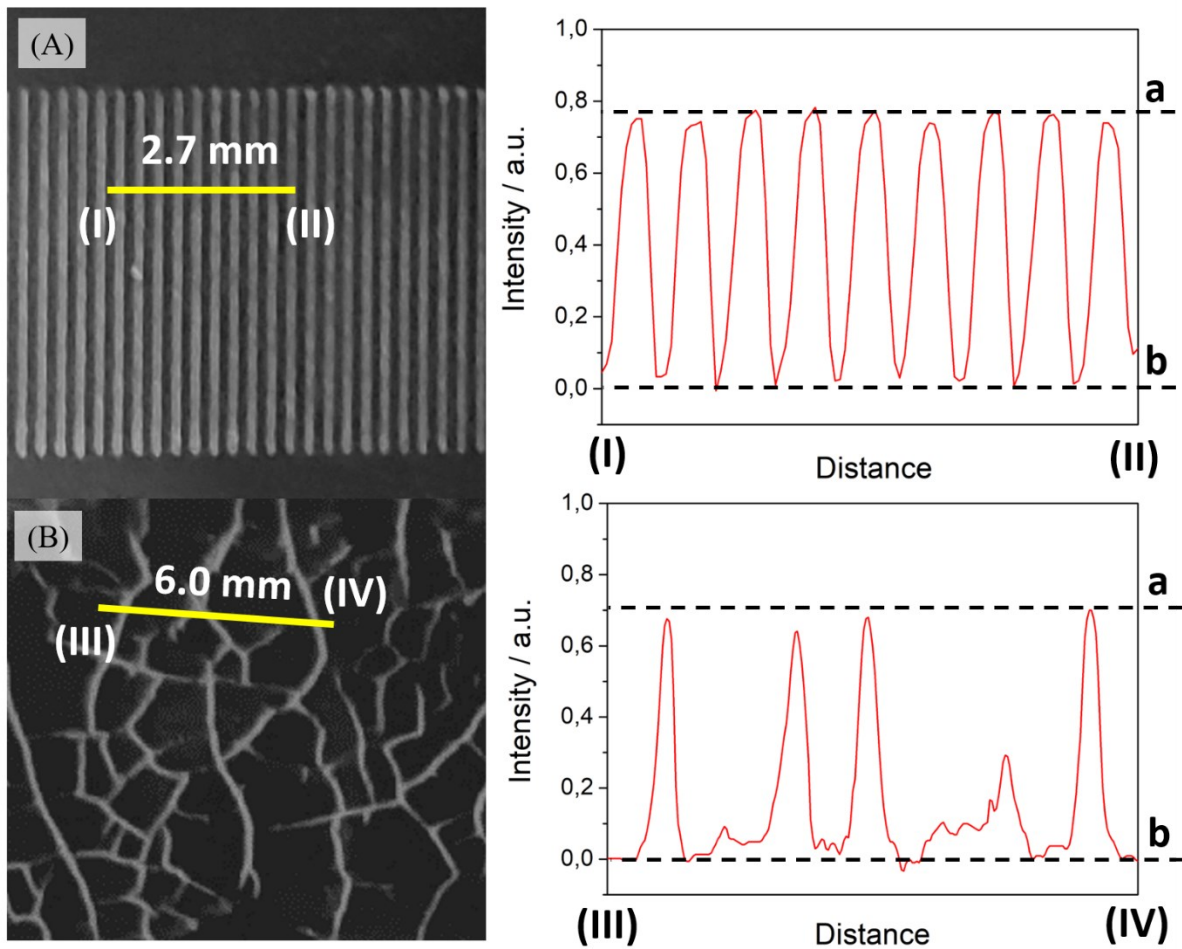
Binary image to analyze signal:noise ratio

Figure S14. (A) Using binary image, a cross section of an official high coercivity magnetic stripe employed for MPI Bath Evaluation with inter stripe separation of 300 µm does not show any kind of background noise, b, and shows a good signal:noise ratio, a/b. (B) Using binary image, a cross section of Reference block (disc with coarse and fine cracks in the surface, produced by grinding and stress corrosion) does not show any kind of background noise again, b, and shows a good signal:noise ratio, a/b.
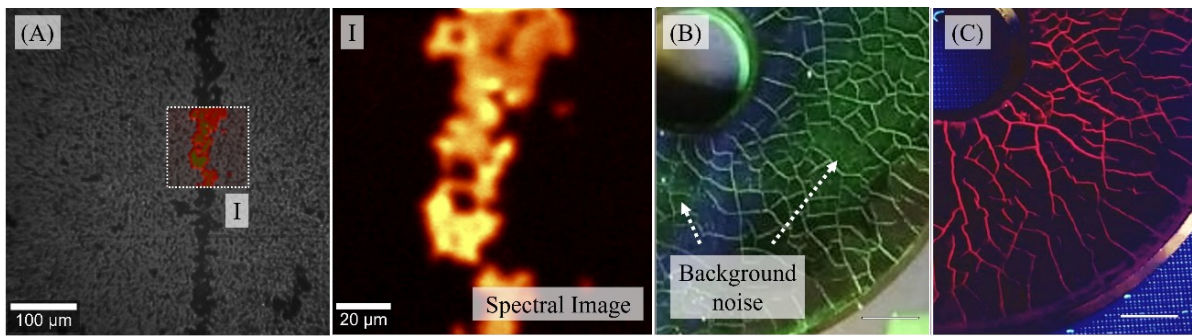
Raman Confocal Microscopy employed for MPI

Figure S15. (A) Optical image by Raman confocal microscopy of one magnetic line from an official high coercivity magnetic stripe employed for MPI Bath Evaluation with inter stripe separation of 300 μm highlighting a specific region under 488 nm excitation proving the specificity of the clustered multifunctional magneto-fluorescent superstructure after washing with acetone (I). (B) Reference Block with conventional green probe (19146, 18970, 15591) provided by Metal-Chek under 470 nm excitation. Low intensity and background noise. (Scale bar: 5mm) (C) Another Reference Block with MghNP@QD under 470 nm excitation. High intensity and no background noise. (Scale bar: 5mm).

There are two types of reference block (type 1 and type 2). The reference block type 1 (used in this manuscript) is a disc with 2 types of natural cracks in the surface. It shall contain coarse cracks and fine cracks produced by grinding and stress corrosion. The block is permanently magnetized by a central conductor through the hole. Evaluation of a detection media is made by visual or other appropriated method of comparison of the indications. **Material preparation**: using steel (Grade 90MnCrV8) the surfaces shall be plane ground to (9,80 ± 0,05) mm then hardened at (860 ± 10) °C for 2 h and quenched in oil to give a surface hardness 63 HRC to 70 HRC. **Process:** grind at a velocity of 35 m/s, using grit size 46J7 with infeed of 0,05 mm per surface, indexing 2,0 mm. Block oxidize at 145 °C to 150 °C for 1,5 h. **Magnetization**: magnetization shall be achieved using a central conductor and direct current at a value of 1 000 A (peak). All the reference blocks are uniquely identified conform Draft International Standard ISO/DIS 9934-2 (ISO/TC 135/SC 2) and this as an advantage comparing with other type of visual analysis. However, it is important to say that the visual characterization is a common and cheap procedure and can be applied with complementary techniques as showed in Figure S15.
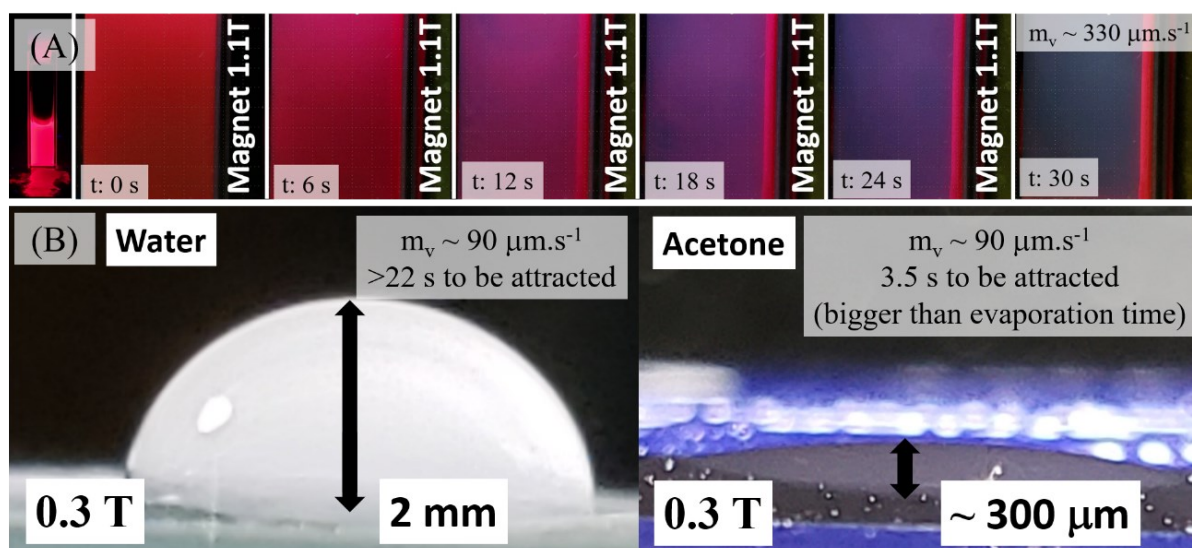
Magnetophoresis of MghNP@QD

Figure S16. (A) Magnetophoretic study of the MghNP@QD to obtain displacement velocity. (B) Drop formation study from water and acetone corroborating the conveniency of using acetone as the solvent in the MPI analysis.

References:

(1)   Melo, F. M.; Grasseschi, D.; Brandão, B. B. N. S., Fu, Y.; Tome, H. E. Superparamagnetic maghemite-based CdTe quantum dots as efficient hybrid nanoprobes for water-bath magnetic particle inspection. ACS *Applied Nano Materials* **2018**, *1*, 2858-2868.

(2)   Mathew, D. S., Juang, R. S. An overview of the structure and magnetism of spinel ferrite nanoaprticles and their synthesis in microemulsions, *Chemical Engineering Journal*, **2007**, 129, *51*-63.